Matter

Article

Pyrolyzed preceramic precursors to compositionally complex ceramics

Graphical abstract

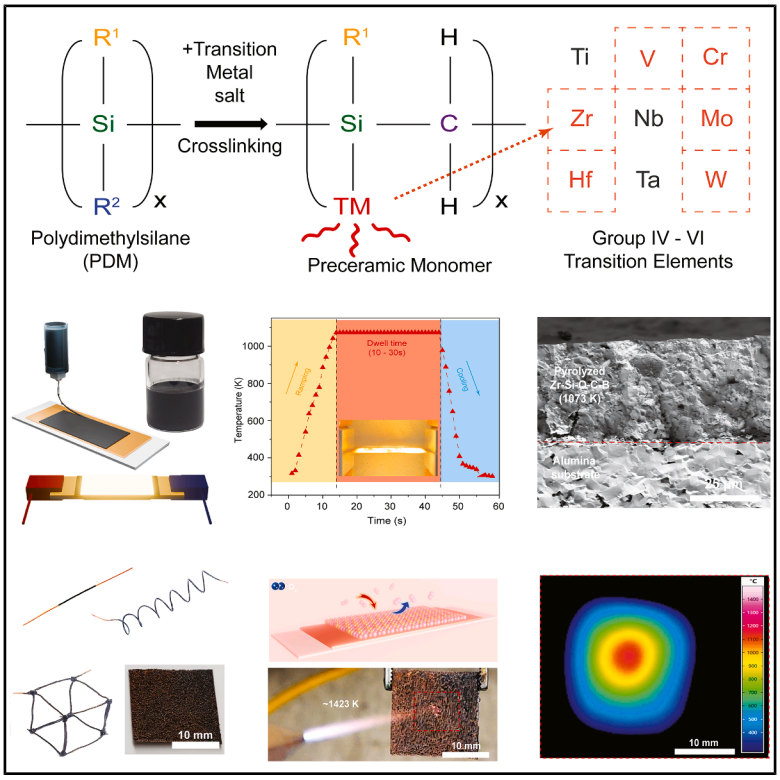

Highlights

- Compositionally tunable system enables tailored structural performance
- Rapid air sintering of ceramic coatings achieved in under 1 min
- Forms dense, oxidation-resistant ceramics via sub-minute air sintering at >1,300 K
- Scalable, additive-free process compatible with complex substrates

Authors

Saurabh Khuje, Jiayue Sun, Chong Yang, ..., Taylor J. Woehl, Liangbing Hu, Shenqiang Ren

Correspondence

liangbing.hu@yale.edu (L.H.), sren@umd.edu (S.R.)

In brief

This work introduces a rapid, scalable route to fabricating compositionally complex ceramic coatings from polymer and metal precursors. The approach eliminates the need for inert atmospheres or long sintering cycles, enabling structural and functional control in a single step. These coatings exhibit exceptional thermal and oxidative stability, with broad relevance to extreme-environment applications in aerospace, electronics, and energy.

1 Discovery
A new material or phenomena

Khuje et al., 2025, Matter 8, 102285
November 5, 2025
Published by Elsevier Inc.
https://doi.org/10.1016/j.matt.2025.102285

CellPress

Please cite this article in press as: Khuje et al., Pyrolyzed preceramic precursors to compositionally complex ceramics, Matter (2025), https://doi.org/10.1016/j.matt.2025.102285

Matter

CellPress
OPEN ACCESS

Article

Pyrolyzed preceramic precursors to compositionally complex ceramics

Saurabh Khuje,[1] Jiayue Sun,[2] Chong Yang,[3] Zhongxuan Wang,[1] Long Zhu,[1] Tangyuan Li,[3] Gianna Valentino,[1] Nicholas Ku,[5] Andres Bujanda,[5] Jian Yu,[5] Tucker Moore,[5] Taylor J. Woehl,[2] Liangbing Hu,[3,4,*] and Shenqiang Ren[1,6,*]

[1]Department of Materials Science and Engineering, University of Maryland, College Park, MD 20742, USA
[2]Department of Chemical and Biomolecular Engineering, University of Maryland, College Park, MD 20742, USA
[3]Department of Electrical and Computer Engineering, Yale University, New Haven, CT 06511, USA
[4]Center for Materials Innovation, Yale University, New Haven, CT 06511, USA
[5]DEVCOM Army Research Laboratory, Aberdeen Proving Ground, MD 21005, USA
[6]Lead contact
*Correspondence: liangbing.hu@yale.edu (L.H.), sren@umd.edu (S.R.)
https://doi.org/10.1016/j.matt.2025.102285

PROGRESS AND POTENTIAL This work presents a transformative, rapid method for fabricating compositionally complex ceramic coatings from preceramic polymers and metal precursors. The resulting materials exhibit a unique combination of high emissivity, low electrical resistivity, excellent oxidation resistance, and mechanical durability, making them ideal for extreme-environment applications across the aerospace, electronics, and energy sectors. Notably, the synthesis route allows air sintering in under a minute, a simplification over conventional high-temperature, inert-atmosphere processing. This is enabled by a compositionally tunable system of polymer-derived ceramics, which incorporate multiple metallic precursors and passive fillers to impart both protective and functional properties. Beyond the synthesis, this study demonstrates the ability to engineer and spatially control metallic phases within the ceramic matrix. This control enhances structural integrity and thermal shock resistance and allows compositional tailoring for application-specific performance. Crucially, the materials do not require sintering additives or external pressure during conversion, enabling scalable fabrication on non-planar and temperature-sensitive substrates. The potential of these coatings is further validated using a high-flux oxygen-hydrogen torch test, where the ceramics effectively prevent oxidation of underlying copper even at surface temperatures exceeding 1,300 K. Furthermore, post-conversion resistivity measurements provide insight into the degree of ceramic transformation and coating uniformity, serving as a convenient quality control metric. This work charts a new direction for ceramic coatings: multifunctional, rapidly deployable, and environmentally robust. The ambient-compatible processing route, which is adaptable to diverse metal systems, unlocks the possibility of on-demand, site-specific fabrication of engineered ceramics. It redefines not only how ceramic materials are made but also where and under what conditions they can be deployed, pushing the frontier of protective materials into new operational domains.

SUMMARY

Ceramics from chemically distinct preceramic polymers offer unique shaping and microstructural control but face challenges such as shrinkage, uncontrolled porosity, and pyrolysis-sensitive stoichiometry. The high-temperature potential of compositionally complex ceramics is further constrained by precursor scarcity and the low-throughput nature of pyrolysis. Here, we introduce short-chain preceramic precursors crosslinked with group IV–VI transition metals (Zr, Cr, V, Mo, Hf, W, Nb, etc.), which are compatible with additive manufacturing. We explored extrusion and ultrafast pyrolysis with multi-metal precursors to enable enhanced compositional complexity, lower processing temperatures, and rapid screening of oxidation-resistant ceramics. Through ultrafast electrical pyrolysis, these crosslinked precursors convert into dense, multiphase ceramics in under a minute. The resulting materials exhibit homogeneous composition and oxidation resistance up to 1,873 K, offering a scalable route to protective coatings and bulk ceramics for extreme environments.

Please cite this article in press as: Khuje et al., Pyrolyzed preceramic precursors to compositionally complex ceramics, Matter (2025), https://doi.org/10.1016/j.matt.2025.102285

INTRODUCTION

There is a growing demand for advanced materials with intricate geometries that can withstand extreme environments.[1,2] Compositionally complex ceramics stand out due to their high-temperature stability, highly distorted lattices, and unique combination of metallic, covalent, and ionic bonding.[3,4] The traditional ceramic powder approach offers limited compositional flexibility and often leads to heterogeneity due to broad particle size distribution and insufficient interfacial connections between particles. The ceramics obtained from chemically distinct preceramic polymer precursors (PCPs) usually feature a combination of shaping and manufacturing with the chemical composition and microstructural control not achievable by other methods. In addition, the PCPs have gained significant attention due to their ability to tailor the polymer composition at the molecular scale, with the ability to further develop complex compositions and thus form metastable compositions following pyrolysis.[5,6] However, the distinctive drawbacks of PCPs are the shrinkage and structural integrity of nano-domain transformation by pyrolysis, uncontrolled porosity from significant gas release (a drastic density change), and pyrolysis-sensitive stoichiometry of multi-elemental atoms in compositionally complex ceramics.[7] These have a substantial impact on the thermo-mechanical characteristics of the formed structure, as they tend to lack adequate oxidation resistance at high temperatures.[8] Furthermore, these Si-based PCPs conventionally use long-chain polymers, making it challenging to incorporate different elements uniformly along the polymer backbone or crosslink different species, as transition elements tend to distribute non-uniformly along the polymeric chains. Furthermore, the decomposition temperature of these polymers is directly proportional to the polymeric chain length.[9,10] Moreover, PCPs require higher pyrolysis temperatures that need protective environments (>1,000°C),[11,12] which causes issues with high throughput and scalability.[13] While metal-modified PCPs have been previously explored, prior work typically involved single-metal systems with limited loading, non-uniform distribution, and high pyrolysis temperatures.[14–16] This calls for new preceramic chemistry, particularly at the nanometric level, with new pyrolysis processes to attain a preceramic green body in a dense ceramic. Here, we introduce a multi-metal, short-chain preceramic approach enabling homogeneous metal incorporation, lower pyrolysis temperatures, and rapid densification. Unlike previous studies focused on conventional single-metal PCPs, our approach utilizes multi-metal crosslinked short-chain precursors, enabling low-temperature rapid densification, enhanced compositional complexity, and extrusion-based shaping capabilities rather than true additive manufacturing.

In this study, we demonstrate a preceramic molecular approach based on the crosslinking of transition metal salts with short-chain preceramic precursors alongside electrical pyrolysis to demonstrate the extrudability and shape processability of these precursors toward forming compositionally complex ceramics exhibiting high-temperature stability. It is important to note that additive manufacturing in this work is employed primarily to demonstrate the processability of the new precursors rather than representing a novelty in printing technology itself.[17] The use of short-chain preceramic precursors rather than long-chain polymers enables greater control of the transition metal dispersion on an atomic level, which also promotes the interaction of filler particles for the formation of dense, pore-free ceramics. We crosslinked transition metal elements from groups 4–6 to short-chain preceramic precursors, resulting in compositionally complex ceramics, which can be electrically pyrolyzed at lower temperatures within a short time span. Furthermore, although ultrafast pyrolysis methods are established, here they are leveraged as a high-throughput screening tool to explore composition-dependent oxidation resistance in these new multi-metal systems. As proof of concept, we crosslink zirconium (IV) chloride ($ZrCl_4$) to polydimethylsilane (PDM) along with zirconium diboride (ZrB_2). Following pyrolysis at just 1,073 K for 1 min in air, we achieve Zr-Si-O-C-B ceramics that are dense and nearly pore free, with multiple homogenously dispersed phases in the final structure that promote greater high-temperature stability. Furthermore, additional transition metals, including hafnium (Hf), vanadium (V), chromium (Cr), molybdenum (Mo), and tungsten (W), were explored as crosslinking elements, alongside additional filler including hafnium diboride (HfB_2), tantalum carbide (TaC), niobium carbide (NbC), and titanium diboride (TiB_2), thus demonstrating the universality of this approach. These ceramics can be extruded as coatings onto various metal or conformal surfaces to enable thermal management of the metal base via suppressing oxidation at elevated temperatures (as a demonstration, a resistivity change from 1.36×10^{-5} Ω.cm at 293 K to 2.61×10^{-5} Ω.cm at 1,422 K was observed for a copper metal base coated with a thin ceramic film). The ceramic film exhibits excellent stability when exposed to temperatures of 1,873 K in the air. Besides thin-film coatings, the feedstock can also be used to fabricate bulk ceramic pellets. Furthermore, the speed and scalability of ceramic formation enable rapid screening of different compositions, such as oxidative barrier coatings on metals or other intricate structures. This could enable the rapid discovery of novel protective ceramics that can be utilized for a broad range of applications taking place under extreme conditions.

RESULTS AND DISCUSSION

Figure 1A presents the synthesis scheme for the multi-element, compositionally complex preceramic precursor, outlining the step-by-step synthesis process. Starting materials include PDM alongside selected metallic salts: zirconium (IV) chloride, molybdenum (III) oxide, tungstosilicic acid hydrate, hafnium (IV) chloride, and vanadium (III) chloride. The PDM converts to polycarbosilane (PCS; a polymeric precursor for silicon carbide) through a reflux reaction[18] and thermally crosslinks with metallic salts to form a transition-metal-crosslinked preceramic polymer, designated as *M*-PCS. For this study, we selected $ZrCl_4$ salt, thus designating *M* as Zr in the *M*-PCS precursor source, which, after thermal curing, exhibits a yellow color. Additional individual transition metal salts, including chromium (Cr), hafnium (Hf), molybdenum (Mo), and vanadium (V), that were crosslinked with PCS to expand the design space for transition-metal-crosslinked preceramic polymers are detailed in Figure S1. For the synthesis of a multi-transition element precursor, zirconium (Zr), hafnium (Hf), and

Please cite this article in press as: Khuje et al., Pyrolyzed preceramic precursors to compositionally complex ceramics, Matter (2025), https://doi.org/10.1016/j.matt.2025.102285

CellPress
OPEN ACCESS

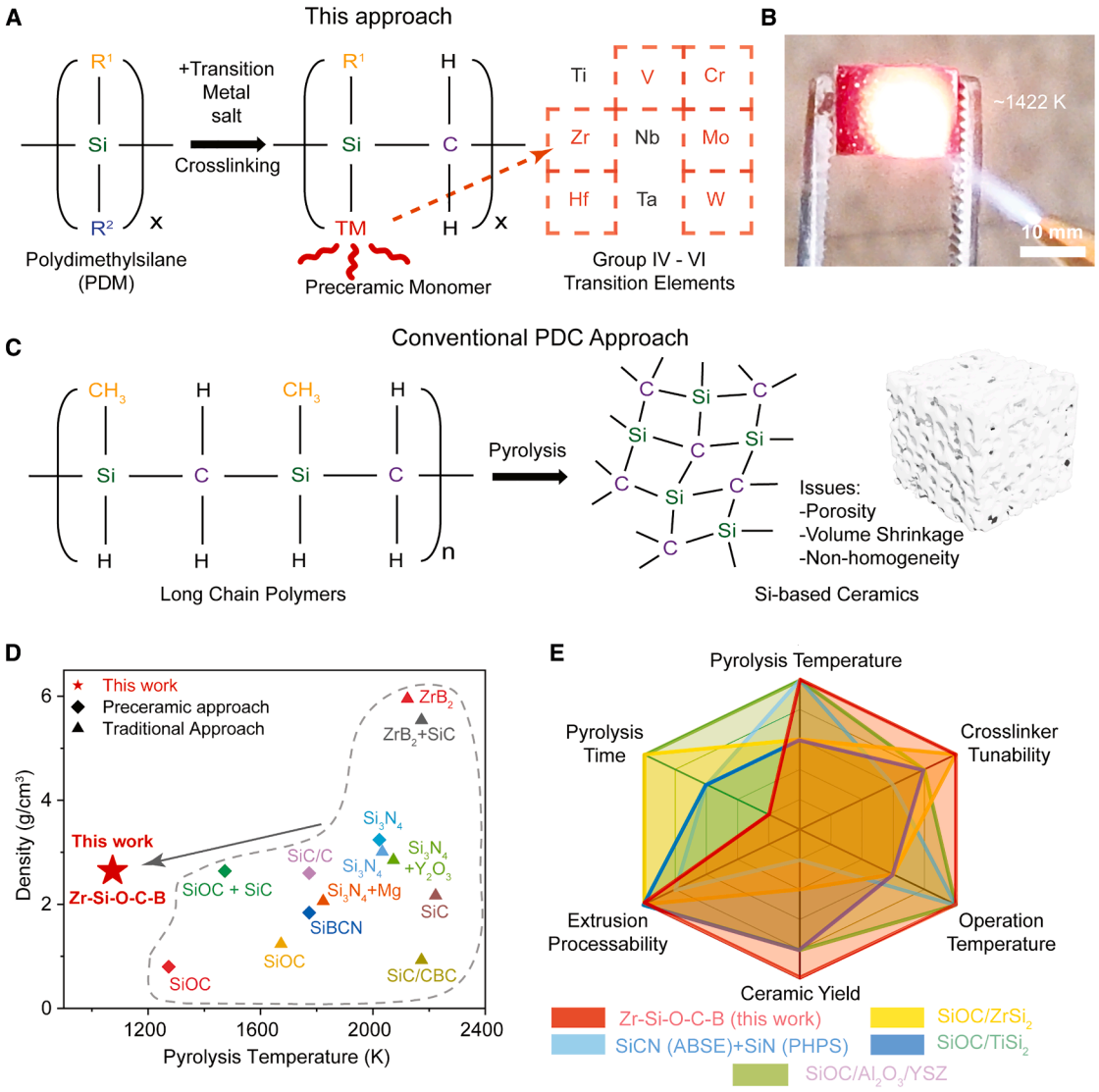

Figure 1. Schematic process for multi-element ceramic material discovery

(A) Process illustrating the approach for the synthesis of a transition-metal-crosslinked precursor toward formation of a single-source high-throughput preceramic polymer precursor. The chemical structure shown corresponds to polydimethylsilane (PDM), the starting material prior to crosslinking. The table depicts transition metals (in red) that can be utilized for this purpose.

(B) Formed ceramics being subjected to oxygen-hydrogen torch with the ceramic coating stable under 1,422 K.

(C) Process depicting the conventional approach toward synthesis of polymer-derived ceramics for comparison.

(D) Ashby plot depicting the characteristic density as a consequence of different pyrolysis temperatures for different techniques. Comparison for materials included this work are as follows. Preceramic approach: SiOC,[19] SiBCN,[20] SiOC/SiC,[21] SiC/C,[22] and Si_3N_4.[23] Traditional approach: SiOC,[24] SiC,[25] SiC/CBC,[26] Si_3N_4 + Mg,[27] Si_3N_4,[28] Si_3N_4 + Y_2O_3,[29] ZrB_2 + SiC,[30] and ZrB_2.[31]

(E) A radar chart illustrating comparison between performance variables for flash-sintered ceramics (this work) and literature for SiCN (ABSE) + SiN (PHPS),[32] SiOC/$TiSi_2$ (expansion agent),[33] Si_3N_4,[34] SiOC/$ZrSi_2$ (active filler),[35] and SiOC/Al_2O_3/YSZ.[36]

chromium (Cr) were crosslinked with PCS through a thermal curing process. Elemental distribution within this complex precursor was subsequently analyzed and visualized via energy-dispersive X-ray spectroscopy (EDS) mapping, as shown in Figure S2. The preceramic precursor slurry consists of the transition-metal-crosslinked preceramic polymer and ZrB_2 filler particles. Figure 1B illustrates the electrical pyrolysis process for ceramic synthesis, which has been optimized for applications in extreme environments using an oxygen-hydrogen torch to achieve temperatures exceeding 1,422 K. This high-temperature process under harsh conditions is further demonstrated in Video S1, which captures the dynamic thermal responses occurring during pyrolysis. For comparison, Figure 1C illustrates the conventional pathway for synthesizing polymer-derived ceramics (PDCs), which primarily relies on silicon-based polymers with extended polymeric chains. Upon pyrolysis under high temperatures in inert

Please cite this article in press as: Khuje et al., Pyrolyzed preceramic precursors to compositionally complex ceramics, Matter (2025), https://doi.org/10.1016/j.matt.2025.102285

atmospheres, these polymers convert to silicon-based ceramics. Figure 1D presents an Ashby plot, contrasting various ceramic manufacturing methods by pyrolysis temperature and resultant ceramic density. Notably, ceramics produced via the approach in this work achieve significantly lower pyrolysis temperatures while maintaining a density comparable to those derived from silicon-based preceramic polymers and traditional ceramic processes. Figure 1E presents a radar chart that compares key performance metrics, such as pyrolysis temperature, pyrolysis duration, extrusion-based processability, crosslinker tunability, ceramic yield, and operational temperature for thermal management, between the PDCs developed in this study and those reported in the literature. Notably, the ceramics produced in this work demonstrate enhanced ceramic yield, improved extrusion-driven shape control, customizable crosslinker options, rapid pyrolysis capability, and robust oxidation resistance at elevated operating temperatures.

Preceramic polymers typically have a low molecular weight, resulting in a relatively low ceramic yield when they are subjected to pyrolysis. To prevent the evaporation of oligomers during pyrolysis, crosslinking of the precursor into macro-molecules with tightly interlocked backbones is beneficial.[34] Figure 2A displays the initial precursor material with added $ZrCl_4$ as the transition metal source. The inset in Figure 2A presents a scanning electron microscopy (SEM) image of the Zr-PDM precursor prior to crosslinking, with energy-dispersive spectroscopy (EDS) elemental mapping in Figure 2B revealing a distinct separation between $ZrCl_4$ and PDM particles. After the crosslinking reaction, the precursor transforms into Zr-PCS, as shown in Figure 2C. The inset in Figure 2C provides a SEM image of the Zr-PCS material post-crosslinking, with EDS mapping (Figure 2D) demonstrating uniform elemental distribution throughout, confirming successful crosslinking. Figures S3 and S4 present both low- and high-magnification SEM images, along with individual EDS elemental maps for the Zr-PCS sample, highlighting the distribution of Zr, Si, and C following the crosslinking reaction. This multi-scale characterization verifies the homogeneous distribution of elements within the sample, underscoring the effectiveness of the crosslinking process. When selecting fillers for the preceramic polymer, it is crucial to prioritize ceramic yields that exceed 75%, as it is necessary to minimize weight loss and shrinkage of the polymer during pyrolysis since PCPs with fillers result in a high ceramic yield and densification. To this extent, we hybridize Zr-PCS (the crosslinked preceramic polymer) with ZrB_2 filler particles to improve the ceramic yield and further enhance its high-temperature stability. Figure S5 displays the X-ray diffraction (XRD) characterization of precursors containing various transition metals, Cr, Hf, Mo, V, and W, designated as "*M*" in *M*-PCS, incorporated with ZrB_2 filler particles post-pyrolysis to identify the resulting phases. This analysis was conducted to assess the versatility and compatibility of the process across different transition elements. The addition of ZrB_2 filler also facilitates electrified Joule heating due to its conductive nature, ranging from 6 to 23 μΩ.cm at room temperature, as seen in Figure S6. Figure 2E presents an optical image of the Zr-Si-O-C-B powder obtained through the pyrolysis of Zr-PCS powder combined with ZrB_2 filler particles. Additionally, a preceramic precursor incorporating Hf as the transition metal, crosslinked with PCS and mixed with ZrB_2 filler particles, was synthesized. Characterization by SEM and EDS mapping confirmed the presence and distribution of individual elements (Hf, Zr, Si, O, C, and B), as shown in Figure S7. The inset at the bottom of Figure 2E displays a SEM image post-pyrolysis, highlighting the morphology of the powder after filler particle incorporation. In addition to ZrB_2, other filler materials—hafnium diboride (HfB_2), tantalum carbide (TaC), niobium carbide (NbC), and titanium diboride (TiB_2)—were evaluated for their compatibility with the synthesis approach detailed in this study. XRD analysis of preceramic precursors based on Zr-PCS combined with various fillers (HfB_2, NbC, TaC, and TiB_2) was performed to verify the universal adaptability of this processing method and to identify the phases formed post-pyrolysis, as shown in Figure S8. Figure 2F presents EDS elemental mapping of a homogeneous cluster of Zr-Si-O-C-B particles, which is further supported by a transmission electron microscopy (TEM) image with an EDS overlay in Figure S9. Figures S10 and S11 provide additional SEM images at low and high magnifications, along with EDS maps, confirming the distribution of elements within Zr-Si-O-C-B particles following pyrolysis at 1,673 K. The inset at the top of Figure 2F illustrates the precursor powder yield at varying pyrolysis temperatures, demonstrating that the inclusion of ZrB_2 particles significantly mitigates weight loss, reducing it to ∼7–10 wt %, a notable improvement compared to the thermal curing process of Zr-PCS. However, it should be noted that the pyrolyzed powder at this stage remains porous and is subsequently subjected to ultrafast electrical pyrolysis to achieve full densification and extrusion-based architectural shaping of the ceramic material.

To confirm the crosslinking reaction, Fourier transform infrared spectroscopy (FTIR spectroscopy) analysis of the precursor is presented in Figure 2G. The spectrum includes pure PDM, Zr-PDM prior to crosslinking, and the resulting Zr-PCS following the crosslinking process, highlighting the structural changes induced by crosslinking. The absorption peaks are observed at 3,403 cm^{-1}, assigned to O-H stretching (trace moisture absorption)[37]; 2,948 and 2,982 cm^{-1}, corresponding to CH_3 stretching; 1,606 cm^{-1}, corresponding to C=C stretching in terminal vinyl groups ($CH=CH_2$)[38]; 1,397 cm^{-1}, corresponding to CH_2 deformation in Si-CH_2-Si; 2,087 cm^{-1}, corresponding to Si-H stretching[39]; and 1,244 cm^{-1}, corresponding to Si-CH_3 deformation and were introduced by PDM. Moreover, 1,080 cm^{-1} has been assigned to CH_2 bending in Si-CH_2-Si, 827 cm^{-1} to Si-C stretching, and 730 cm^{-1} to Si-C stretching in Si-CH_3.[40] It should be noted that dehydrochlorination (*M*-Cl/Si-H) leads to the incorporation of Zr into PCS chains.[41] The Zr cations are crosslinked with the PCS chain via the mechanism of dehydrochlorination (Zr-Cl/Si-H), which leads to the consumption of Si-H groups. Additionally, hydrosilylation reactions between Si-H and C=C bonds occur, leading to the consumption of C=C groups, as evidenced by the significant reduction of the 1,606 cm^{-1} peak after crosslinking into Zr-PCS. This observation corroborates the fact that the introduction of Zr acts as a catalyst for hydrosilylation reactions.[42] Moreover, compared to Zr-PDM powder, there is a significant reduction in absorption peaks, specifically at 3,403 cm^{-1}, further indicating the crosslinking of Zr-PCS. Figure S12 presents the FTIR spectroscopy spectra of various transition metals after crosslinking with PCS, which was

Please cite this article in press as: Khuje et al., Pyrolyzed preceramic precursors to compositionally complex ceramics, Matter (2025), https://doi.org/10.1016/j.matt.2025.102285

CellPress
OPEN ACCESS

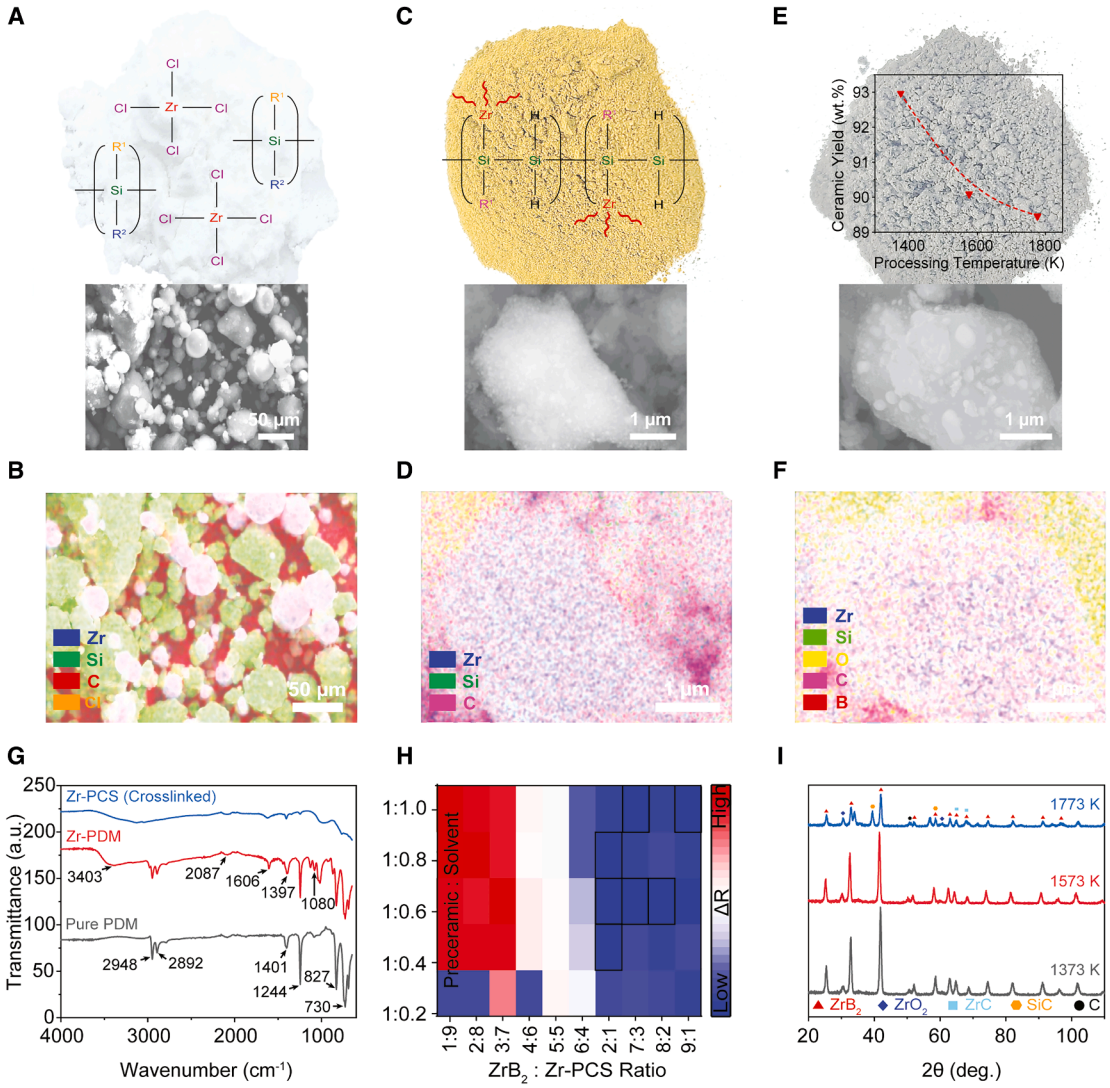

Figure 2. Characteristics of preceramic polymer prior to the addition of filler particles

(A) Optical image of the Zr-PDM starting material prior to crosslinking. Inset: SEM observation of segregated $ZrCl_4$-PDM particles.

(B) EDS mapping of the $ZrCl_4$-PDM mixture prior to crosslinking. The Zr signal appears weak due to poor dispersion and agglomeration of $ZrCl_4$ within the polymer matrix.

(C) Optical image of the Zr-PCS following crosslinking. Inset: SEM observation of a cluster of Zr-PCS particles.

(D) EDS mapping of the crosslinked Zr-PCS cluster showing uniform distribution of Zr, Si, and C, confirming successful integration of Zr into the polymeric precursor.

(E) Optical image of the Zr-Si-O-C-B precursor following addition of filler particles. Inset: (top) plot depicting the ceramic yield corresponding to different processing temperatures. (Bottom) SEM of a cluster of Zr-Si-O-C-B powder.

(F) EDS mapping of Zr-Si-O-C-B powder is indicative of homogeneous distribution of elements.

(G) FTIR spectroscopy for pure PDM powder, Zr-PDM prior to crosslinking, and Zr-PCS crosslinked after thermal curing.

(H) Heatmap illustrates the results of the screening study for determining the optimum ratio for preceramic powder and solvent.

(I) Plot depicting the pyrolysis temperature-dependent XRD for Zr-Si-O-C-B powders.

conducted to verify successful crosslinking. The spectra provide insight into the chemical transformations associated with the crosslinking process across different transition metal precursors.

Due to the growing chemical complexity of the search for preceramic-derived ceramics, the number of possible combinations is too vast for an Edisonian method to be feasible. A screening method for the determination of precursor feedstock could significantly suppress the processing times with accelerated material development. Leveraging the ratios between Zr-PCS, ZrB_2 filler particles, and the solvent, we utilized the resistance change (ΔR) of the ceramic-coated copper layer between room temperature and 1,273 K as the criterion for screening in this study. For screening purposes, we identified ten different weight

Please cite this article in press as: Khuje et al., Pyrolyzed preceramic precursors to compositionally complex ceramics, Matter (2025), https://doi.org/10.1016/j.matt.2025.102285

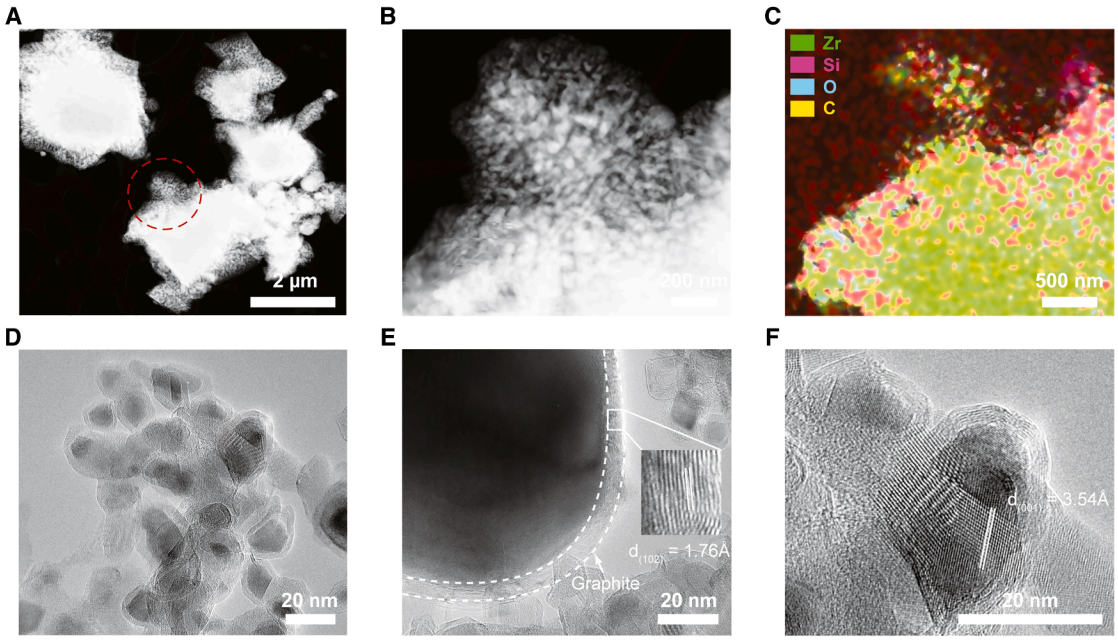

Figure 3. TEM characterization of Zr-Si-O-C-B ceramics

(A) Low-magnification STEM image.

(B) Dark-field STEM image of a cluster of Zr-Si-O-C-B particles. Scale bar represents 200 nm.

(C) EDS analysis showing the spatial distribution of Zr, Si, O, C, and B within the ceramic precursor, highlighting elemental dispersion and indicating the uniformity and phase interactions in the ceramic matrix.

(D) HRTEM image of the Zr-Si-O-C-B preceramic precursor signifying a core-shell structure.

(E) HRTEM image showing ZrB_2 particles encapsulated by a crystalline graphitic carbon layer, revealing the core-shell structure and the ordered carbon phase.

(F) HRTEM analysis revealing lattice fringes of ZrB_2, highlighting the (002) planes with an interplanar spacing of 3.54 Å, indicating preserved crystalline order in the ZrB_2 phase.

ratios of ZrB_2 and Zr-PCS powders (1:9, 2:8, 3:7, 4:6, 5:5, 6:4, 7:3, 8:2, 9:1, and 2:1) with five weight ratios of solvents (0.2, 0.4, 0.6, 0.8, and 1 wt %) in combination with each ZrB_2:Zr-PCS ratio. Figure S13 displays optical images of the sample batch prepared for high-throughput evaluation. As shown in Figure 2H, a higher weight ratio of ZrB_2 filler particles enhances high-temperature stability, while an increased solvent ratio facilitates the accelerated fabrication of samples when combined with electrical pyrolysis, optimizing both stability and manufacturability. From the heatmap, ZrB_2:Zr-PCS ratios of 2:1 with solvent ratios of 0.4 (ΔR = 0.44), 0.6 (ΔR = 0.33), and 0.8 (ΔR = 0.42) wt %; 7:3 with solvent ratios of 0.6 (ΔR = 0.28) and 1 (ΔR = 0.38) wt %; 8:2 with solvent ratios of 0.6 wt % (ΔR = 0.31); and 9:1 with solvent ratios of 1 wt % (ΔR = 0.47) had the lowest ΔR, the values for which are listed in Table S1. We selected the ZrB_2:Zr-PCS ratio of 2:1 with a solvent ratio of 0.6 wt % for the purpose of this study. Figure 2I shows the XRD analysis patterns for the powders pyrolyzed at different temperatures. From the plot, multiple phases can be identified, namely, ZrB_2, ZrO_2, ZrC, SiC, and C.[43–45] The presence of ZrB_2, ZrC, and ZrO_2 can be attributed to the reaction of Zr with PCS and the solvent. Additionally, PCS primarily forms silicon carbide, graphite, and/or carbon at elevated temperatures.

To elucidate the microstructure of the Zr-Si-O-C-B ceramics, TEM and STEM were employed. Low-magnification TEM images (Figures 3A and S14–S16) reveal micron-sized clusters formed after pyrolysis of the preceramic precursor with ZrB_2 fillers, comprising particles ranging from 20 to 100 nm (Figure 3B). The TEM-EDS mapping (Figure 3C) provides a detailed spatial distribution of Zr, Si, O, and C elements, highlighting the incorporation of Zr within the matrix and the presence of Si, O, and C at the shell layer. Additional EDS maps (Figures S17–S21) further corroborate these findings across different regions of the sample. High-resolution TEM (HRTEM) imaging (Figure 3D) distinguishes the crystalline ZrB_2 phase from the surrounding matrix. The HRTEM analysis reveals that the ZrB_2 nanoparticles are encapsulated within a graphitic carbon layer, forming a core-shell structure. The presence of graphene-like domains is supported by the observation of lattice fringes at d(102) = 1.76 Å (Figure 3E), indicative of ordered carbon structures.[46] Figure S22 provides additional HRTEM images showcasing the crystalline coating around ZrB_2 particles. Meanwhile, lattice fringes at d(002) = 3.54 Å (Figure 3F) correspond to the (002) planes of ZrB_2, confirming the retention of crystalline integrity in the ZrB_2 cores following pyrolysis. This structural heterogeneity contributes to the material's thermal stability and oxidation resistance, with the graphitic carbon shell providing a barrier against thermal degradation.[47] At elevated temperatures (up to 1,673 K), further decomposition of the surrounding phases leads to the formation of turbostratic carbon, a less ordered variant of graphite and SiC phases, while preserving the crystallinity of ZrB_2. The resulting hybrid microstructure, which integrates

graphene-like carbon with ZrB_2 cores, enhances the material's thermal conductivity and mechanical robustness, maintaining structural integrity under extreme conditions.[48] The coexistence of graphitic carbon and crystalline ceramic phases highlights their intricate interaction, resulting in a composite with superior stability and functionality under high-temperature conditions.

The dispersible nature of preceramic materials enables the precise tuning of rheological properties, allowing the liquid preceramic precursor to be deposited through extrusion-based methods. Figure 4A illustrates the extrusion-assisted deposition process, showcasing the synthesis and application of the printable slurry for producing dense ceramic films. An optical image of the extrusion-based slurry deposition process, where the preceramic slurry is deposited onto a copper substrate, is provided in Figure S23. Modified electrical current-assisted sintering is further employed for rapid pyrolysis of the preceramic slurry by applying a DC electric field within a short time span, as opposed to hours at elevated temperatures in conventional processing methods. This effect can be explained via Joule heating at the local grain boundaries, enhancing the diffusion of the grain boundaries (kinetic effect) while inhibiting grain growth (thermodynamic effect). With the synergistic combination of higher temperatures at the grain boundaries and smaller grain sizes, the sintering rate is significantly improved, as can be observed in Video S2. Figure 4B illustrates the temperature-time profile of the electrical pyrolysis process at a power setting of 40 W. A dwell time of approximately 10–30 s at the target temperature facilitates densification, enabling the entire pyrolysis process to be completed within 60 s, with printed copper serving as the conductive substrate. The inset in Figure 4B provides an optical image of the electrical pyrolysis process, which is further demonstrated in Video S3. Figure 4C displays XRD diffractograms collected from samples subjected to electrical pyrolysis at various power inputs, highlighting phase evolution with changing power levels. From the plot, four distinct phases were revealed: ZrB_2, ZrO_2, ZrC, and SiC.[44] These phases arise from a composite effect where a combination of two distinct phases results in a third, synergistic phase that enhances the thermal stability and reliability of the ceramic coatings at elevated temperatures. Additionally, XRD diffractograms for preceramic slurries incorporating various transition metals (Cr, Hf, Mo, V, and W) after electrical pyrolysis are presented in Figure S24, demonstrating the method's adaptability across multiple compositions. Figure S25 further validates this universal approach by showcasing XRD diffractograms for Zr-PCS-based slurries with different fillers post-electrical pyrolysis. Figure 4D provides a cross-sectional SEM view of the electrically pyrolyzed ceramics, revealing a dense microstructure free of cracks or pores. Figure S26 offers additional SEM images at varying magnifications of the Zr-Si-O-C-B sample post-pyrolysis, supported by EDS mapping, in Figure S27, which visualizes the uniform element distribution within this compositionally complex ceramic. Figure 4E presents SEM images of a sample subjected to electrical pyrolysis at 1,073 K. Additional plane-view SEM images of preceramic slurries containing various transition metals (Cr, Hf, Mo, V, and W) after electrical pyrolysis are shown in Figures S28 and S29. The SEM observations indicate that as the pyrolysis temperature increases from 556 K, surface uniformity progressively improves, with no substantial changes observed beyond 1,073 K. EDS mapping for the 1,073 K sample performed at 30 W confirms the presence and uniform distribution of Zr, Si, O, C, and B elements, as depicted in Figure S30. Additionally, adhesion testing was conducted according to ASTM D3359 standards on the electrically pyrolyzed Zr-Si-O-C-B sample, with the results shown in Figure S31. A crosshatch pattern was created on the coating surface using a standard cutter tool, followed by the application and removal of 3M Scotch Magic Tape. The test revealed partial coating removal corresponding to a 3B rating, indicating moderate adhesion strength between the ceramic film and the copper substrate. Figure 4F presents a density plot for samples pyrolyzed at various temperatures, demonstrating an increase in ceramic film density with increasing pyrolysis temperatures attributed to the enhanced particle packing achieved at higher temperatures.

Taking into consideration the liquid nature of the extrudable preceramic slurry coupled with the swift and adaptive capability of the electrical pyrolysis process, we evaluate the coating conformability onto different copper geometries and tantalum metal foil for this work. Figure 5A shows the optical images depicting the conformability of the preceramic precursor on 1D, 2D, and 3D geometries, corroborating its versatility in conformal deposition across geometrically intricate surfaces, with the optical images of the plane (non-coated) and isometric views (coated with preceramic slurry and electrically pyrolyzed) presented in Figures S32 and S33. Additionally, the preceramic feedstock can be compacted and pyrolyzed to obtain bulk monolithic samples, and the optical image of the bulk monolithic pellet prepared by compacting preceramic feedstock followed by electrical pyrolysis is presented in Figures S34–S43. Figure 5B (top) shows an optical image of the ceramic-coated copper foam being subjected to the oxygen-hydrogen flame to examine its oxidation resistance. The formed ceramic coating prevents oxygen molecules from diffusing inwards toward the metallic (copper) layer. Figure 5B (bottom) shows the infrared image of the ceramic-coated copper foam under the influence of the oxygen-hydrogen torch, reaching temperatures above 1,423 K. Figure 5C (top) shows the SEM images of the Cu-foam before and after torch tests, with no visible morphological changes to the surface. To further elucidate the robustness of this material for thermal management, an Ashby plot consisting of operating temperature vs. coating thickness was compiled and is presented in Figure S44. From the plot, it can be inferred that the ceramic synthesized in this work displays robust performance at higher operating temperatures. Furthermore, the formed ceramics are exposed to high temperatures (1,073–1,773 K) to determine any phase changes and confirm their thermal stability, as seen in Figures S45–S47. Figure 5C (bottom) shows the XRD plot of Zr-Si-O-C-B before and after exposure to elevated temperatures, confirming its high-temperature reliability to withstand exposure above 1,273 K with no signs of degradation or oxidation. Furthermore, ceramic coatings with different transition elements were also evaluated for oxidation stability, and the results are compiled in Table S2. As seen from the results, the Cr, Mo, and W samples perform considerably well, with an average resistance change of 5% for the ceramic formed using W as the transition element. For the evaluation of the oxidation stability of

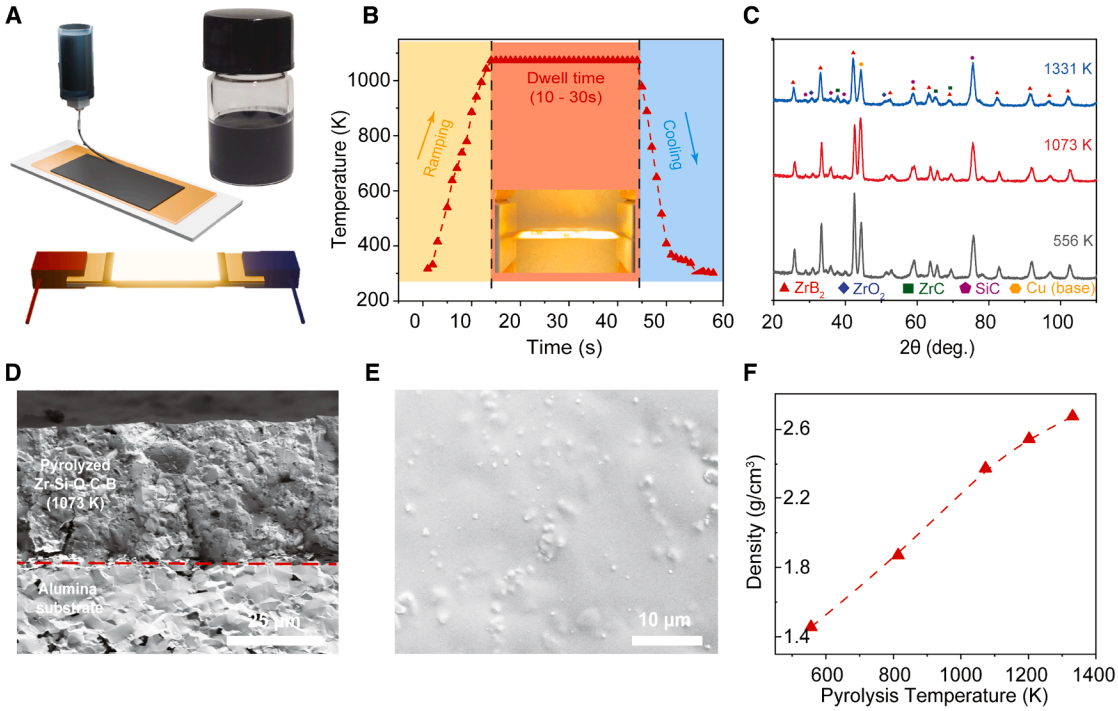

Figure 4. Extrusion-based deposition and flash pyrolysis of preceramic precursors to form ceramics

(A) Scheme depicting the extrusion-assisted deposition of preceramic slurry (left) and optical image of the preceramic slurry (right). Scheme depicting the electrical pyrolysis process for fabricating ceramics (bottom).

(B) Temperature-time profile for electrical pyrolysis durations with copper substrate. Inset: optical image of the sample during electrical pyrolysis with tantalum metal foil.

(C) Plot depicting power-dependent XRD patterns for electrically pyrolyzed ceramic coatings.

(D) SEM observation of the cross-section of electrically pyrolyzed sample at 1,073 K.

(E) SEM observation of the plane view of sample electrically pyrolyzed at 1,073 K.

(F) Plot depicting the resulting density as a result of increasing pyrolysis temperature for fabricated ceramics.

the ceramic at higher temperatures (>1,423 K), Figure 5D (top) shows the scheme illustrating Zr-Si-O-C-B coated on the tantalum foil as a demonstration. Figure 5D (bottom) illustrates the working mechanism depicting the ceramic layer functioning as a diffusion barrier to oxygen molecules, thus preventing oxidation of the ceramic as well as the underlying metal layer. Figure 5E shows the SEM observation of the ceramic layer on tantalum foil exposed to a temperature of 1,873 K for a duration of 5 min under atmospheric conditions. The sample was inserted at the set temperature for varying durations, and no visible morphological changes can be observed on the surface, indicating robust stability without phase separation, erosion, or oxidation even after exposure at elevated temperatures. Figure 5F shows the EDS mapping of the sample exposed for a duration of 5 (top) and 30 (bottom) min, respectively, at 1,873 K, and it can be inferred that the ceramic film maintains its homogeneity and displays no phase separation or oxidation, thus corroborating the robust nature of the compositionally complex ceramics developed in this work. The bulk pellet samples were also evaluated for their oxidation stability by exposing them to a temperature of 1,273 K for varying durations (1, 10, 30, and 60 min, respectively) under oxidative atmospheric conditions. Following high-temperature exposure, the samples were cross-sectioned for SEM and EDS analysis. As shown in Figures S48–S51, the bulk Zr-Si-O-C-B pellet exhibits no signs of oxidation or phase separation, demonstrating its stability under extreme conditions.

Conclusion

Herein, we present a methodology for synthesizing short-chain preceramic precursors capable of crosslinking group IV–VI transition metals (including Zr, Cr, V, Mo, Hf, W, and Nb), enabling the formation of compositionally complex ultrahigh-temperature ceramics. This approach combines extrusion-based slurry deposition with electrical pyrolysis, achieving rapid, pressure-free conversion of preceramic materials into dense ceramics at 1,073 K in ambient air within 1 min. This process supports the incorporation of diverse elements into the preceramic network, resulting in ceramics with tailored compositions and minimal shrinkage or porosity upon pyrolysis. The pyrolyzed ceramics exhibit a dense microstructure and contain multiple phases. The presence of these distinct phases contributes to a synergistic enhancement of the material's stability and reliability under high-temperature conditions. The 1D, 2D, and 3D metallic architectures coated with these ceramic layers demonstrate exceptional thermal management capabilities, maintaining

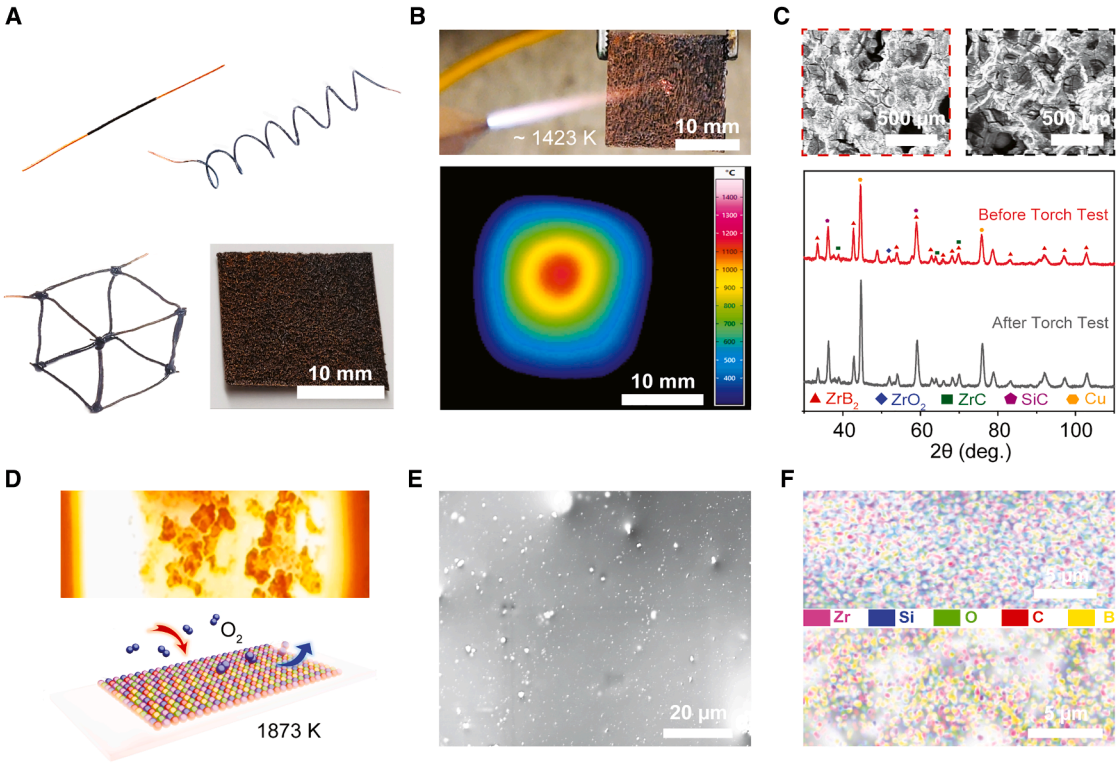

Figure 5. Evaluation of formed ceramic structures for high-temperature stability

(A) Optical images of ceramic-coated copper geometries (1D, 2D, and 3D) for potential high-temperature thermal management applications.

(B) Ceramic-coated copper foam being subjected to oxygen-hydrogen flame with no significant change to the surface (top). The infrared (IR) image was captured by means of a thermographic camera for the ceramic-coated Cu-foam subjected to oxygen-hydrogen torch (bottom).

(C) SEM observations of ceramic-coated Cu-foam before and after torch testing (top). Corresponding XRD plot elucidating the crystallographic structure for ceramic-coated copper before and after torch testing is shown (bottom). Scale bar represents 500 μm.

(D) Optical image of the high-temperature setup for determination of oxidation stability of ceramic-coated tantalum foil (top). Scheme depicting the working mechanism for oxidation and corrosion-resistant extreme environment coatings with ceramic layers for thermal management is shown (bottom).

(E) Planar-view SEM observation of the ceramic sample exposed to a temperature of 1,873 K under atmospheric conditions for a duration of 5 min on tantalum foil.

(F) EDS mapping of the ceramic sample exposed to a temperature of 1,873 K under atmospheric conditions for a duration of 5 (top) and 30 (bottom) min. Scale bar represents 5 μm.

high-temperature structural integrity. Moreover, the ability to apply the preceramic coating uniformly to various conductive surfaces allows for the formation of protective ceramic layers that effectively shield metals from oxidation even at temperatures as high as 1,873 K. While extrusion-based deposition and ultrafast pyrolysis are established techniques, their integration with newly developed multi-metal short-chain precursors enables the rapid discovery and fabrication of complex, oxidation-resistant ceramics. This method provides a pathway for producing ceramics with complex transition metal compositions, as well as enabling the creation of bulk monoliths and coatings. It opens new avenues for the development of advanced ceramic materials suited for aerospace, energy, and defense applications, where thermal stability and durability are paramount.

METHODS

PCP preparation

Zirconium (IV) chloride (*or* hafnium (IV) chloride, vanadium (III) chloride, chromium (III) chloride, molybdenum trioxide, or tungstosilicic acid hydrate) was mixed with PDM in varying ratios (1:1, 2:1, 3:1, 4:1, and 5:1, with the left value representing the weight of PDM and the right value representing the weight of zirconium (IV) chloride) and processed at a temperature of 743 K in a tube furnace under a nitrogen environment with a ramping rate of 5°C/min, followed by natural cooling. This process enabled the conversion of PDM to PCS and the crosslinking of the transition metal with the preceramic polymer network. Subsequently, the obtained feedstock was further mixed with zirconium diboride (or hafnium diboride, tantalum carbide, niobium carbide, and titanium diboride) powder in varying ratios (for high-throughput testing) and sintered at different temperatures (1,373–1,773 K) in a tube furnace under a nitrogen environment, again with a ramping rate of 5°C/min, followed by natural cooling to obtain the final feedstock powder for further processing.

Coating of precursor slurry and electrical pyrolysis (copper and tantalum as substrates)

Following sintering of the compositionally complex ceramic powder, the powder was ground to finer particles, and a solvent

(StarPCS SMP-10 polymer) was added in different ratios. The resulting slurry was deposited onto alumina substrates coated with copper nanoplates. A Keithley 2260B-80-40 DC power supply was used for electrical pyrolysis (for the conversion of the preceramic precursor to ceramic) of the samples in atmospheric conditions via variation in the power supplied, which varied the temperature. For pyrolysis of the tantalum foil sample, the Gleeble 563 thermal mechanical simulator was employed. The system was environmentally controlled for three cycles of rough vacuuming and ultrahigh purity argon purging. We used 0.150-mm-thick tantalum foil as our substrate, held in place by water-cooled copper grips, and used a dual-color pyrometer for temperature control. The sample was heated from 273 to 1,773 K in <40 s, with a holding time of ~30 s, and then allowed to cool naturally.

Testing and characterization

The electrical readings were characterized using a Keithley 2450 SourceMeter with an oxygen-hydrogen gas flame generator as the heating source and platinum wires as electrodes. High-temperature steady-state testing was carried out using a 1,700°C tube furnace (TCH Instruments). SEM characterization was carried out using a Hitachi SU-70 scanning electron microscope. XRD was performed with Thermo-Fisher ARL Equinox 100 XRD. TEM/STEM and EDS characterizations were carried out using a JEOL JEM-2100F transmission electron microscope equipped with a Bruker Quantax Xflash6 EDS detector operating at a 200 kV acceleration voltage.

RESOURCE AVAILABILITY

Lead contact

Further information and requests for resources and reagents should be directed to and will be fulfilled by the lead contact, Shenqiang Ren (sren@umd.edu).

Materials availability

Preceramic materials and the ceramics generated in this study will be made available upon request, but we may require a completed materials transfer agreement if there is potential for commercial application.

Data and code availability

Any additional information required to reanalyze the data reported in this paper is available from the lead contact upon request.

ACKNOWLEDGMENTS

The authors acknowledge the financial support provided by the Army Research Office (W911NF2520056).

AUTHOR CONTRIBUTIONS

S.R. designed and supervised the project. S.K. worked on the synthesis of metal-based PDC precursor powder and sample preparation via electrical pyrolysis. S.K. and L.Z. worked on the SEM imaging of the sample. J.S. worked on the TEM characterization of the sample. S.K. worked on the structural and electrical characterization via high-temperature testing of the material. G.V. assisted with the flash sintering of ceramic coating on tantalum metal. S.K., T.L., A.B., L.H., and S.R. worked on revising the manuscript draft.

DECLARATION OF INTERESTS

The authors have filed a patent application related to the technology presented in this work.

SUPPLEMENTAL INFORMATION

Supplemental information can be found online at https://doi.org/10.1016/j.matt.2025.102285.

Received: March 7, 2025
Revised: June 10, 2025
Accepted: June 16, 2025

REFERENCES

1. Jayan, K.D. (2023). Recent Advances in Ultra-High-Temperature Ceramic Coatings for Various Applications. Ceramic Coatings for High-Temperature Environments: From Thermal Barrier to Environmental Barrier Applications (Springer Nature), pp. 409–440.
2. Wang, B., Wang, C., Yu, X., Cao, Y., Gao, L., Wu, C., Yao, Y., Lin, Z., and Zou, Z. (2022). General synthesis of high-entropy alloy and ceramic nanoparticles in nanoseconds. Nat. Synth. 1, 138-146.
3. Wright, A.J., and Luo, J. (2020). A step forward from high-entropy ceramics to compositionally complex ceramics: a new perspective. J. Mater. Sci. *55*, 9812–9827.
4. Cao, G., Liang, J., Guo, Z., Yang, K., Wang, G., Wang, H., Wan, X., Li, Z., Bai, Y., Zhang, Y., et al. (2023). Liquid metal for high-entropy alloy nanoparticles synthesis. Nature *619*, 73–77.
5. Deng, B., Wang, Z., Chen, W., Li, J.T., Luong, D.X., Carter, R.A., Gao, G., Yakobson, B.I., Zhao, Y., and Tour, J.M. (2022). Phase controlled synthesis of transition metal carbide nanocrystals by ultrafast flash Joule heating. Nat. Commun. *13*, 262.
6. Wang, H., Chen, X., Gao, B., Wang, J., Wang, Y., Chen, S., and Gou, Y. (2013). Synthesis and characterization of a novel precursor-derived ZrC/ZrB2 ultra-high-temperature ceramic composite. Appl. Organomet. Chem. *27*, 79–84.
7. Colombo, P., Mera, G., Riedel, R., and Sorarù, G.D. (2010). Polymer-derived ceramics: 40 years of research and innovation in advanced ceramics. J. Am. Ceram. Soc. *93*, 1805–1837.
8. Wright, A.J., Wang, Q., Huang, C., Nieto, A., Chen, R., and Luo, J. (2020). From high-entropy ceramics to compositionally-complex ceramics: A case study of fluorite oxides. J. Eur. Ceram. Soc. *40*, 2120–2129.
9. Heinze, D., Mang, T., Popescu, C., and Weichold, O. (2016). Effect of side chain length and degree of polymerization on the decomposition and crystallization behaviour of chlorinated poly (vinyl ester) oligomers. Thermochim. Acta *637*, 143–153.
10. Hotza, D., Nishihora, R.K., Machado, R.A.F., Geffroy, P.M., Chartier, T., and Bernard, S. (2019). Tape casting of preceramic polymers toward advanced ceramics: A review. Int. J. Ceramic Engine. & Sci. *1*, 21–41.
11. Bernardo, E., and Colombo, P. (2007). Advanced oxide ceramics from a preceramic polymer and fillers. Soft Mater. *4*, 175–185.
12. Colombo, P., Bernardo, E., and Parcianello, G. (2013). Multifunctional advanced ceramics from preceramic polymers and nano-sized active fillers. J. Eur. Ceram. Soc. *33*, 453–469.
13. Wang, X., Schmidt, F., Hanaor, D., Kamm, P.H., Li, S., and Gurlo, A. (2019). Additive manufacturing of ceramics from preceramic polymers: A versatile stereolithographic approach assisted by thiol-ene click chemistry. Addit. Manuf. *27*, 80–90.
14. Yang, N., and Lu, K. (2021). Effects of transition metals on the evolution of polymer-derived SiOC ceramics. Carbon *171*, 88–95.
15. Cai, T., Qiu, W.F., Liu, D., Han, W.J., Ye, L., Zhao, A.J., and Zhao, T. (2013). Synthesis, characterization, and microstructure of hafnium boride-based composite ceramics via preceramic method. J. Am. Ceram. Soc. *96*, 1999–2004.
16. Ionescu, E., Papendorf, B., Kleebe, H.J., Poli, F., Müller, K., and Riedel, R. (2010). Polymer-derived silicon oxycarbide/hafnia ceramic nanocomposites. Part I: phase and microstructure evolution during the ceramization process. J. Am. Ceram. Soc. *93*, 1774–1782.

17. Eckel, Z.C., Zhou, C., Martin, J.H., Jacobsen, A.J., Carter, W.B., and Schaedler, T.A. (2016). Additive manufacturing of polymer-derived ceramics. Science *351*, 58–62.
18. Lodhe, M., Babu, N., Selvam, A., and Balasubramanian, M. (2015). Synthesis and characterization of high ceramic yield polycarbosilane precursor for SiC. J. Adv. Ceram. *4*, 307–311.
19. Barsoum, M. (2019). Fundamentals of Ceramics (CRC press)).
20. Li, S., Duan, W., Zhao, T., Han, W., Wang, L., Dou, R., and Wang, G. (2018). The fabrication of SiBCN ceramic components from preceramic polymers by digital light processing (DLP) 3D printing technology. J. Eur. Ceram. Soc. *38*, 4597–4603.
21. Friedel, T., Travitzky, N., Niebling, F., Scheffler, M., and Greil, P. (2005). Fabrication of polymer derived ceramic parts by selective laser curing. J. Eur. Ceram. Soc. *25*, 193–197.
22. Windsheimer, H., Travitzky, N., Hofenauer, A., and Greil, P. (2007). Laminated object manufacturing of preceramic-paper-derived Si? SiC composites. Adv. Mater. *19*, 4515–4519.
23. Altun, A.A., Prochaska, T., Konegger, T., and Schwentenwein, M. (2020). Dense, strong, and precise silicon nitride-based ceramic parts by lithography-based ceramic manufacturing. Applied Sciences *10*, 996.
24. Li, J., and Lu, K. (2015). Highly porous SiOC bulk ceramics with water vapor assisted pyrolysis. J. Am. Ceram. Soc. *98*, 2357–2365.
25. Jana, D.C., Barick, P., and Saha, B.P. (2018). Effect of sintering temperature on density and mechanical properties of solid-state sintered silicon carbide ceramics and evaluation of failure origin. J. Mater. Eng. Perform. *27*, 2960–2966.
26. Chen, W., and Miyamoto, Y. (2014). Fabrication of porous silicon carbide ceramics with high porosity and high strength. J. Eur. Ceram. Soc. *34*, 837–840.
27. Bowen, L.J., Weston, R.J., Carruthers, T.G., and Brook, R.J. (1978). Hot-pressing and the α-β phase transformation in silicon nitride. J. Mater. Sci. *13*, 341–350.
28. Yeh, H. (1979). private communication and Yeh, HC and PF Sikora Bull. Am. Ceram. Soc *58*, 444.
29. Yeheskel, O., Gefen, Y., and Talianker, M. (1984). Hot isostatic pressing of Si 3 N 4 with Y 2 O 3 additions. J. Mater. Sci. *19*, 745–752.
30. Chamberlain, A.L., Fahrenholtz, W.G., Hilmas, G.E., and Ellerby, D.T. (2004). High-strength zirconium diboride-based ceramics. J. Am. Ceram. Soc. *87*, 1170–1172.
31. Zhang, S.C., Hilmas, G.E., and Fahrenholtz, W.G. (2006). Pressureless densification of zirconium diboride with boron carbide additions. J. Am. Ceram. Soc. *89*, 1544–1550.
32. Günthner, M., Kraus, T., Dierdorf, A., Decker, D., Krenkel, W., and Motz, G. (2009). Advanced coatings on the basis of Si (C) N precursors for protection of steel against oxidation. J. Eur. Ceram. Soc. *29*, 2061–2068.
33. Torrey, J.D., and Bordia, R.K. (2008). Processing of polymer-derived ceramic composite coatings on steel. J. Am. Ceram. Soc. *91*, 41–45.
34. Riffard, F., Joannet, E., Buscail, H., Rolland, R., and Perrier, S. (2017). Beneficial effect of a pre-ceramic polymer coating on the protection at 900° C of a commercial AISI 304 stainless steel. Oxid. Met. *88*, 211–220.
35. Wang, K., Günthner, M., Motz, G., and Bordia, R.K. (2011). High performance environmental barrier coatings, Part II: Active filler loaded SiOC system for superalloys. J. Eur. Ceram. Soc. *31*, 3011–3020.
36. Tian, Z., Zhu, W., Yan, X., and Su, D. (2022). Passive Filler-Loaded Silicon Oxycarbide Coating on Nickle Alloy with High Thermal Shocking Behavior and Oxidation Resistance. Materials *15*, 6395.
37. Socrates, G. (2004). Infrared and Raman Characteristic Group Frequencies: Tables and Charts (John Wiley & Sons).
38. Pavia, D., Lampman, G., Kriz, G., and Vyvyan, J. (2012). Introduction to Spectroscopy Fourth edition. Cram 101 Learning system (Cengage Learning).
39. Arkles, B., and Launer, P. (1987). Infrared analysis of organosilicon compounds: spectra-structure correlations. Silicon Compounds Register and Review, Second edition. (Gelest, Inc.).
40. Yu, Z., Zhan, J., Zhou, C., Yang, L., Li, R., and Xia, H. (2011). Synthesis and characterization of SiC (Ti) ceramics derived from a hybrid precursor of titanium-containing polycarbosilane. J. Inorg. Organomet. Polym. Mater. *21*, 412–420.
41. Yu, Z., Pei, Y., Lai, S., Li, S., Feng, Y., and Liu, X. (2017). Single-source-precursor synthesis, microstructure and high temperature behavior of TiC-TiB2-SiC ceramic nanocomposites. Ceram. Int. *43*, 5949–5956.
42. Marciniec, B. (2013). Comprehensive Handbook on Hydrosilylation (Elsevier).
43. Putz, H., and Brandenburg, K. (2016). Match!–Phase Analysis Using Powder Diffraction, Crystal Impact. GbR, Kreuzherrenstr *102*, 53227.
44. Savyak, M.P., and Melnick, A.B. (2020). Peculiarities of Refractory Borides Formation during Mechanical Alloying IV-V Group Transition Metals with Boron in Planetary Mill. In Recent Advances in Boron-Containing Materials, Metin Aydin, ed. (IntechOpen).
45. Clarkson, C.M., Wyckoff, C., Parvulescu, M.J.S., Rueschhoff, L.M., and Dickerson, M.B. (2022). UV-assisted direct ink writing of Si3N4/SiC preceramic polymer suspensions. J. Eur. Ceram. Soc. *42*, 3374–3382.
46. Asl, M.S., and Balak, Z. (2023). Fabrication and Characterization of ZrB2 Ceramic in Presence of Graphite Platelet and SiC. Silicon *15*, 6911–6919.
47. Das, S., Sozal, M.S.I., Li, W., and John, D. (2023). Ultra-High-Temperature Ceramic Coatings ZrC, ZrB2, HfC, and HfB2. In Ceramic Coatings for High-Temperature Environments: From Thermal Barrier to Environmental Barrier Applications, A. Pakseresht and K.K. Amirtharaj Mosas, eds. (Springer), pp. 441–469.
48. Li, H., Zhang, L., Zeng, Q., Wang, J., Cheng, L., Ren, H., and Guan, K. (2010). Crystal structure and elastic properties of ZrB compared with ZrB2: A first-principles study. Comput. Mater. Sci. *49*, 814–819.